In-situ V_p/V_s ratio reveals fault-zone material variation at the westernmost Gofar transform fault, East Pacific Rise

Tianze Liu[1], Jianhua Gong[1], Wenyuan Fan[1], & Guoqing Lin[2]

[1]Institute of Geophysics and Planetary Physics, Scripps Institution of Oceanography, UC San Diego
[2]Department of Marine Geosciences, Rosenstiel School of Marine, Atmospheric, and Earth Science, University of Miami

Key Points:

- Rupture barrier zone has a moderate V_p/V_s ratio of 1.75–1.80.
- Down-dip edge of the 2008 $M6$ mainshock has a low V_p/V_s ratio of 1.61–1.69.
- V_p/V_s ratio in the rupture barrier zone increased in the nine months before the mainshock.

Corresponding author: Tianze Liu, `tianzeliu@ucsd.edu`

Abstract

Ocean transform faults often generate characteristic earthquakes that repeatedly rupture the same fault patches. The westernmost Gofar transform fault quasi-periodically hosts $\sim M6$ earthquakes every ~ 5 years, and microseismicity suggests that the fault is segmented into five distinct zones, including a rupture barrier zone that may have modulated the rupture of adjacent $M6$ earthquakes. However, the relationship between the systematic slip behavior of the Gofar fault and the fault material properties is still poorly known. Specifically, the role of pore fluids in regulating the slip of the Gofar fault is unclear. Here, we develop a new method using differential arrival times between nearby earthquakes to estimate the in-situ V_p/V_s ratio of the fault-zone materials. We apply this technique to the dataset collected by an ocean-bottom-seismometer network deployed around the Gofar fault in 2008, which recorded abundant microearthquakes, and find a moderate V_p/V_s ratio of 1.75–1.80 in the rupture barrier zone and a low V_p/V_s ratio of 1.61–1.69 in the down-dip edge of the 2008 $M6$ rupture zone. This lateral variation in V_p/V_s ratio may be caused by both pore fluids and chemical alteration. We also find a 5–10 % increase in V_p/V_s ratio in the barrier zone during the nine months before the mainshock. This increase may have been caused by fluid migrations or slip transients in the barrier zone.

Plain Language Summary

Oceanic transform faults are natural laboratory for studying earthquake processes because characteristic earthquakes on them are usually highly repeatable. One such example is the westernmost Gofar transform fault. The fault has two rupture zones regularly generating magnitude 6 earthquakes every 5 to 6 years, which are separated by a barrier zone repeatedly stopping ruptures on the two adjacent segments. One explanation for the barrier zone's distinct behavior is that it consists of different materials from the rupture zones. To explore this hypothesis, we analyze records of thousands of small earthquakes that occurred in 2008 and find that the barrier zone has a higher ratio between P and S velocities than that of the rupture zone. This difference indicates that the materials in the barrier zone and the rupture zone are different in their fluid content and chemical composition, which may have regulated their distinct slip behaviors. We also find an increase in the ratio between P and S velocities in the barrier zone in the nine months before the magnitude 6 earthquake in 2008, which may reflect fluid flows or fault slips in the barrier zone.

1 Introduction

Oceanic transform faults demonstrate some of the most systematic and predictable slip behaviors. Moderate- to large-magnitude characteristic earthquakes often rupture the same fault patches quasi-periodically, which are frequently preceded by systematic foreshock activity (McGuire et al., 2005). This clear earthquake-cycle pattern implies that the underlying physical processes are likely repeatable. Therefore, oceanic transform faults are ideal natural laboratories for studying the mechanisms of earthquake nucleation and arrest (McGuire, 2008; Boettcher & McGuire, 2009). Specifically, their regular cycles provide opportunities to capture anticipated characteristic events and record variations in material properties that may reflect the stress and strength evolution leading to the characteristic earthquakes.

The Gofar transform-fault system at the East Pacific Rise (Fig. 1a) exemplifies such regular earthquake behaviors. The fault system has two short intra-transform spreading centers (ITSC) and three segments with the westernmost segment denoted as G3. The G3 segment, situated between the East Pacific Rise (EPR) in the west and an ITSC in the east (Fig. 1a), regularly hosts $\sim M6$ events every ~ 5 years at two separate asperities (McGuire, 2008). The two asperities are locked interseismically and are connected by a ~ 10 km long rupture barrier zone (hereafter "barrier zone") along strike. The barrier zone seems to have repeatedly stopped the ruptures of $M6$ earthquakes at the locked zones, including the Sep 18, 2008 $M6$ mainshock that occurred west of the barrier zone (Fig. 1a–c; McGuire et al., 2012). The barrier zone is likely highly fractured with a fluid-filled porosity up to 8% and has a ∼10–20% P-wave velocity reduction extending through the whole crust to the uppermost mantle, in contrast to the velocity structure of the rupture zone (Roland et al., 2012; Froment et al., 2014). The average S-wave velocity of the barrier zone decreased by about 3% and then fully recovered within one week prior to the 2008 $M6$ mainshock, showing a dynamic evolution of the material properties (McGuire et al., 2012; Froment et al., 2014). The observed velocity changes are likely related to adjustments of poroelastic properties (e.g., fluid fraction and pore geometry) resulting from stress changes (McGuire et al., 2012). However, details of the along-strike material-property changes remain elusive primarily due to the limited spatial resolution of conventional imaging techniques.

Rock V_p/V_s ratio is sensitive to both the pore fluids and the mineral composition (Christensen, 1996; Takei, 2002). Specifically, in-situ V_p/V_s ratios obtained from differential P and S arrival times of nearby earthquakes are capable of resolving fault-zone material properties with high spatial and temporal resolutions in the near-source regions than conventional tomographic images (Lin & Shearer, 2007, 2009; Lin et al., 2015; Bloch et al., 2018; Lin & Shearer, 2021). For example, Lin et al. (2022) showed that the high-resolution in-situ V_p/V_s ratios are much more complex than the tomographic V_p/V_s models in California and that the in-situ V_p/V_s ratios illuminate the important role of fluids in driving repeating earthquakes.

Here, we use an one-year ocean-bottom-seismometer (OBS) dataset recorded by a 2008 experiment at G3, which captured the anticipated $M6$ characteristic earthquake as well as $\sim 30{,}000$ microearthquakes, to investigate the variation of in-situ V_p/V_s ratio in the fault zone. We design a new method to examine the spatio-temporal evolution of the in-situ V_p/V_s ratio and validate the method with a suite of synthetic tests. We then compare the estimates with predictions from rock-physics models to infer physical processes within the G3 fault zone.

2 Data

We use the data collected by the 2008 Quebrada-Discovery-Gofar marine seismic experiment (McGuire et al., 2012; Roland et al., 2012; Froment et al., 2014). The experiment deployed 40 OBS stations, including 16 broadband seismographs around G3 (triangles in Fig. 1a). Among the 16 stations, three did not record useful data (gray triangles in Fig. 1a), and thus our analysis focuses on the waveforms from the rest 13 stations, which were configured to sample at either 50 Hz or 100 Hz. We use the catalog from Gong and Fan (2022) to estimate the in-situ V_p/V_s ratio of the G3 fault zone. The catalog includes both automated and manually determined locations, and we focus on the 30,854 earthquakes reported in the automated catalog in this study (see Gong and Fan (2022) for details). The earthquakes are mostly within ± 1 km in the strike-normal direction (Fig. 1a). We first obtain both P and S waveforms of the earthquakes, resample the waveforms to 100 Hz, and then bandpass filter the records at 4–20 Hz. The waveforms are windowed from -0.4 to 0.6 s around the predicted P arrivals and -0.8 to 0.7 s around the predicted S arrivals. The predicted P and S arrivals are obtained using an one-dimensional (1D) velocity model extracted from Roland et al. (2012). We cross-correlate the P and S waveforms of each earthquake with those of its closest 100 neighboring events recorded at the same station. The differential P and S traveltimes and cross-correlation coefficients are computed for each event-pair at every available station, but they are only recorded when cross-correlation coefficient of at least one phase is greater than 0.6. We only keep cross-correlation measurements of an event pair if more than five stations can meet the requirement. We note that the recording criteria are loose and additional selection processes are necessary as discussed below. In total, we obtain 8,857,302 differential arrival times for estimating in-situ V_p/V_s ratios.

3 Methods

3.1 Fault Patches of Interest

The $\sim$ 30,000 microearthquakes are nonuniformly distributed within the G3 fault zone. To study the variation of the in-situ V_p/V_s ratio of the G3 fault zone, we focus on ten non-overlapping patches. The selection is primarily guided by the spatio-temporal evolution of seismicity reported in Gong and Fan (2022). The patches differ in their sizes to balance the spatial resolution and a sufficient number of differential arrival times for each patch (Figs. 1b and c). Only one V_p/V_s ratio is estimated for each patch for a time period. For example, we divide the barrier zone into four patches due to its active seismicity, while grouping the east lock zone into one single patch because of its low seismicity. Regardless of the fault patch dimensions, we only use the differential arrival times of event pairs within 2 km to obtain local in-situ V_p/V_s-ratio estimates. OBS data often have inaccurate timing because the instrument clocks are unable to synchronize with satellites. Although a linear clock correction has been applied to the data when the data was archived,the residual nonlinear clock drift may still bias the results (Gouédard et al., 2014). Therefore, we only use event pairs occurring within 30 days to minimize the effects of the clock drifts. We further evaluate the impacts of the maximum event temporal separation in Section 5.1.1.

The eastern G3 hosted an $M6$ event in 2007 (approximately Zone 1 in Gong and Fan (2022); McGuire et al. (2012)). Because this fault segment had only 2,487 earthquakes during the observational period, we group them into one patch (Patch E; Figs. 1b and c). The barrier zone (approximately Zone 2 in Gong and Fan (2022)) includes four patches with two shallow patches F1 and F2 and two deep patches D1 and D2, where the seismicity rate was high before the mainshock but largely halted after the mainshock (Figs. 1b and c). We define two patches M1 and M2 at the down-dip edge of the mainshock rupture zone (approximately Zone 3 in Gong and Fan (2022); the rupture zone is largely quiescent before and after the mainshock), with M1 being seismically active during the whole observation period and M2 consisting mostly aftershocks of the 2008 $M6$ earthquake (Figs. 1b and c). We note that M2 and F1 are spatially close but have distinct temporal patterns of seismicity (Gong & Fan, 2022), which implies a possible difference in material properties. The events immediately west of the mainshock zone are grouped into the patch T (approximately Zone 4 in Gong and Fan (2022)), where a moderate level of seismicity persisted through the observational period (Figs. 1b and c). The $M6$ mainshock may have also ruptured the area above T if the rupture propagated bilaterally (Figs. 1b and c). Near the East Pacific Rise, the western end of G3 hosted a two-week long swarm in December 2008, including two M5 earthquakes ("December swarm" in McGuire et al. (2012); approximately Zone 5 in Gong and Fan (2022)). This segment is divided into two patches S1 and S2 (Figs. 1b and c).

3.2 Preprocessing of Differential Arrival Times

In an ideal case where events occur in a homogeneous medium, and the measurements contain no error or noise, the P and S differential arrival times of event pairs in a compact cluster form a line with zero intercept and a slope equal to the V_p/V_s ratio of the medium (e.g., Figure 3 in Lin and Shearer (2007)). In reality, the event origin times are often not accurate enough, and these event-timing errors will introduce static time shifts to the measured P and S differential arrival times. The time shifts will cause the differential times to form lines with the same slope as the ideal case but varying intercepts for different event pairs (e.g., Figure 5 in Lin and Shearer (2007)). Moreover, because our differential arrival times are computed without analyst reviews, the measurements are susceptible to phase misalignment and other sources of random noise, which could potentially bias the in-situ V_p/V_s-ratio estimates (see Section 5.1.1 for a detailed discussion). For example, the measured differential arrival times for D1 are not only highly scattered but also form a trend with a slope of ~ 1.3, significantly smaller than the V_p/V_s ratios of typical rocks (Fig. 2a). Therefore, we design a preprocessing procedure to reduce the effects of observation errors in differential arrival times before estimating in-situ V_p/V_s ratios (Fig. 3).

We first remove arrival-time measurements with a cross-correlation coefficient less than 0.6 for either P or S wave (e.g., Lin et al., 2007). We define this step as the CC step and the following step as the linearity step because the following steps will further select the measurements based on how well they can be fitted with lines (Fig. 3). We then fit differential arrival times of each event pair with a line while allowing for a non-zero intercept and remove the intercept for the event pair (Fig. 3). For the line fitting, we require a minimum number ($\mathrm{N_{min}}$) of seven data points and keep event pairs with a number of data points greater than the threshold for the following analysis. The threshold is determined as $\mathrm{N_{min}} = 7$ through trial-and-error, and its effect on the in-situ V_p/V_s-ratio estimates will be discussed in Section 4.1. We iteratively fit a line for an event pair using the total-least-square (TLS) regression (also known as "orthogonal-distance regression"; Van Huffel and Vandewalle (1991)), which minimizes the ℓ_2 norm of the misfits for both the P and S differential times. All measurements of an event pair are initially used to estimate a slope and an intercept, and a root-mean-square (RMS) misfit is recorded. If the RMS misfit is below a threshold ($\mathrm{RMS_{max}}$), we retain the measurements, remove the estimated intercept from them, and record the slope estimate as the V_p/V_s ratio estimate for this event pair. Otherwise, we discard the data point with the largest misfit and repeat the line fitting procedure. This iterative process is terminated when the RMS misfit is below $\mathrm{RMS_{max}}$ or the number of measurements of the event pair drops below $\mathrm{N_{min}}$. In the latter case, this event pair will not be used for further analysis. We choose a threshold of $\mathrm{RMS_{max}} = 0.005\,\mathrm{s}$, a strict criterion given the data sampling interval of 0.01 s. This parameter choice aims to retain only the highest-quality differential arrival times for robust estimation. We will also evaluate the effects of different choices of $\mathrm{RMS_{max}}$ in Section 4.1.

We use the joint distribution between the V_p/V_s ratios and differential-P-time ranges (τ) of event pairs to further remove measurement outliers for each fault patch (Fig. 4). The differential-P-time range τ is defined as the difference between the maximum and minimum differential P arrival times ($\tau = \Delta T_{\mathrm{p,max}} - \Delta T_{\mathrm{p,min}}$) for an event pair. For example, Fig. 4 shows the joint distributions for M1 and D1 after the intercept removal step. The distributions show measurements forming apparent strips with $V_p/V_s \approx 0$ and $\tau > 0.15\,\mathrm{s}$ (Fig. 4), which are clearly erroneous and thus excluded from further analysis. The remaining measurements are distributed in $\tau = 0.001$–$0.150\,\mathrm{s}$ and $V_p/V_s =$ 0.5–3 (Fig. 4). This group centers around 1.7 and shows a variation decreasing with increasing τ (Fig. 4). We opt to use event pairs with $V_p/V_s = 0.5$–3 and $\tau = 0.050$–$0.150\,\mathrm{s}$ (solid green boxes in Fig. 4) for estimating V_p/V_s ratios. The V_p/V_s-ratio range in our criteria removes measurements that would lead to erroneous estimates, and the τ limit helps select event pairs with reliable estimates. The lower bound for τ (τ_{min}) is a key parameter because it controls the trade-off between data quantity and quality, and we will discuss its effect in detail in Section 4.1.

The preprocessing procedure removes most of the cross-correlation measurements and retains only a small portion (typically $< 1\%$) of the data points. However, the selected measurements have high quality and likely yield more accurate estimates. For example, the unprocessed measurements of D1 show strong scattering and a trend with a slope of ~ 1.3, whereas the preprocessed measurements yield a best-fitting line with a slope of ~ 1.8 (Figs. 2a and b). Elaborate preprocessing could potentially cause selection biases, i.e., our strict data-selection procedure could bias the V_p/V_s-ratio estimates.

However, we emphasize that the line-fitting step of the preprocessing procedure does not limit the slope (V_p/V_s ratio) values and that the joint-distribution-analysis step selects event pairs in a generous range of $V_p/V_s = 0.5$–3 (Fig. 4). We will further test the effects of the preprocessing procedure on synthetic data to show that it does not introduce biases to the final V_p/V_s-ratio estimates (Section 5.1.1). Among all fault patches, the patches in the swarm zone (S1 and S2) have a remarkably lower fraction of events left for the final V_p/V_s-ratio estimation compared to other patches (Fig. 1d). Besides, the remaining events in F2 after preprocessing are predominantly located in the deeper part of the patch (Fig. 1d). These features are probably because both the swarm and barrier zones have high degrees of structural complexity due to pervasive fracturing, which could lead to incoherent waveforms between events, causing their differential arrival times to have larger errors and thus be eliminated in the preprocessing procedure. We will further discuss the relation between data retention rate and structural complexity in Section 5.3.1.

3.3 Robust V_p/V_s-ratio Estimation

With the selected differential arrival times, we estimate the in-situ V_p/V_s ratio for each fault patch following an iterative approach similar to the line-fitting step in the preprocessing procedure. We first fit a line with zero intercept to the measurements and compute the standard deviation of the misfits and remove the measurements with a misfit greater than two times the standard deviation. We then repeat the line-fitting using the remaining measurements to obtain the final V_p/V_s ratio estimate. This data removal step typically disqualify less than 10% of the measurements, and the V_p/V_s ratios estimated at the two steps are only marginally different (Figs. 2b and c). We further estimate the uncertainties of the V_p/V_s-ratio estimates by computing the standard deviation of the V_p/V_s ratios from 500 bootstrap-resampled datasets. Each bootstrap realization is obtained by randomly drawing the same number of measurements from the original dataset with replacement, allowing the same measurement to be sampled multiple times. We note that the uncertainty estimate from bootstrap resampling provides a measure of data variability yet does not address uncertainties resulting from choices of preprocessing parameters or the spatial resolution of our data and method (Section 5.1). As an example, the final V_p/V_s ratio for D1 is estimated to be 1.799 with an uncertainty of ± 0.006 and an RMS misfit of 0.005 s.

4 Results

4.1 Spatial Variation of In-situ V_p/V_s Ratio

The in-situ V_p/V_s-ratio estimates of the ten fault patches show a distinct spatial variation with values ranging from 1.524 to 1.799. The eastern part of G3, including the barrier zone (F1, F2, D1, and D2) and the eastern locked zone (E), have high V_p/V_s ratios (1.752–1.799), whereas the western part, including the mainshock zone (M1 and M2), the transition zone (T), and the eastern patch of the swarm zone (S2), have low V_p/V_s ratios (1.524–1.693; Fig. 1d). The other fault patch S1 in the swarm zone has a V_p/V_s ratio of 1.777, similar to the patches in the east (Fig. 1d). S1 and S2 have much fewer event pairs for estimating V_p/V_s ratio compared to the other patches probably due to the combined effects of a poor station coverage and dissimilarity of event waveforms (Figs. 1a and d). Due to the low number of measurements, results for S1 and S2 are likely less reliable than those of other fault patches and thus will not be further discussed. We observe a sharp contrast in V_p/V_s ratio between the two adjacent patches M2 and F1, which correlates with the temporal variation of their seismicity (Figs. 1b–d; Gong & Fan, 2022). These observations suggest an abrupt boundary in material properties between the mainshock zone and the barrier zone. The in-situ V_p/V_s ratios, their uncertainties, and associated RMS misfits of all fault patches except for S1 and S2 are summarized in Table S1.

To evaluate the robustness of the observed spatial variation, we examine the effects of N_{min}, RMS_{max}, and τ_{min} on the V_p/V_s ratio estimates. We test the effects of these parameters by only varying one parameter at a time while keeping the other two at our preferred values of $N_{min} = 7$, $RMS_{max} = 0.005$ s, and $\tau_{min} = 0.05$ s, leading to six additional sets of parameter combinations for the eight fault patches (except for S1 and S2; 5). For N_{min}, we test $N_{min} = 5$, 7, and 9 (Figs. 1d and 5a), and the results suggest a negative correlation between the V_p/V_s-ratio estimates and N_{min}. However, the relative differences of the V_p/V_s-ratio estimates remain largely unchanged, indicating that the observed spatial pattern is robust. For example, the V_p/V_s ratios of M2 and F1 both decrease as N_{min} increases from 5 to 9, but the estimate of M2 remains smaller than that of F1 (Figs. 1d and 5a). The general decrease of the estimates with increasing N_{min} may be because a greater N_{min} reduces the number of measurements with large differential-arrival-time values, which have stronger impacts on the V_p/V_s estimates than the measurements closer to the origin. Including large differential-arrival-time measurements could yield more robust estimates because random errors in these measurements are smaller compared with the measurements themselves. The V_p/V_s-ratio estimates for M1, D1, and D2 are largely insensitive to the choice of N_{min} likely due to their more numerous measurements (Figs. 1d and 5a).

We vary RMS_{max} from 0.005 s to 0.015 s and find that the V_p/V_s-ratio estimates are generally insensitive to the choice of the parameter (Figs. 1d and 5b). For τ_{min}, we vary its value from 0.025 to 0.075 s and find that the V_p/V_s-ratio estimates positively correlate with τ_{min}, although the spatial variation of the estimates remain the same (Figs. 1d and 5c). The positive correlation may be because a greater τ_{min} tends to select more measurements with large differential arrival times, which influences the V_p/V_s-ratio estimates in an opposite way to that of N_{min}. This suite of sensitivity tests demonstrates that although the absolute V_p/V_s ratios are affected by the parameters, the resolved spatial variation in V_p/V_s ratio is robust regardless of the preprocessing-parameter choices.

4.2 Temporal Evolution of In-situ V_p/V_s Ratio

The fault patches in the mainshock zone (M1 and M2) and barrier zone (F1, F2, D1, and D2) have sufficient measurements to enable us to evaluate the temporal evolution of V_p/V_s ratios in these segments (Fig. 6). For each fault patch, we group every 50 consecutive event pairs (after preprocessing) into a time window with a temporal increment of 10 event pairs. This scheme creates nonuniform window lengths but an equal number of measurements for each window, which guarantees that the estimates are robust and that the observed temporal variation is not due to a change in sample size. We then estimate the V_p/V_s ratio for each time window and evaluate its temporal variation. Because the temporal variation of seismicity is very different between different patches, the distribution of time windows also varies greatly between them (Fig. 6). Regardless of the time window length, only differential-time measures of event pairs within 30 days are used for estimating V_p/V_s ratios.

The estimated in-situ V_p/V_s ratios fluctuate at all six fault patches albeit with different magnitudes. The V_p/V_s ratio of M1 oscillates within $\pm 3\%$ of the average value and shows no clear trend during the observation period (Figs. 6a and 7b). The V_p/V_s ratio of M2 appears to have decreased $\sim$ 3% after the mainshock, though this change may not be well resolved due to a lack of earthquakes in M2 before the $M6$ mainshock (Figs. 6b and 7b). In contrast, the four barrier-zone patches, F1, F2, D1, and D2, show a greater fluctuation with an apparent increasing trend before the $M6$ mainshock (Figs. 6c–e and 7a). Hereafter, we will use Julian day (abbreviated as d; number of days since Jan 1, 2008) to describe the temporal evolution of the in-situ V_p/V_s ratios. For F1, the V_p/V_s ratio increased by $\sim$ 6% between $\sim$ 60 and $\sim$ 120 d, dropped by $\sim$ 5% between $\sim$ 120 and $\sim$ 160 d, and increased again by $\sim$ 5% between $\sim$ 160 d and the mainshock (Figs. 6c and 7a). For F2, the V_p/V_s ratio increased by $\sim$ 9% between $\sim$ 30 and $\sim$ 100 d, dropped by $\sim$ 5% between $\sim$ 100 and $\sim$ 120 d, and then increased by $\sim$ 3% between $\sim$ 120 and $\sim$ 160 d (Figs . 6d and 7a). Although F2 had abundant microearthquakes before the mainshock, a lower percentage of their differential arrival times passed the preprocessing procedure compared to other barrier-zone patches, resulting in a lack of measurements in the 100 days immediately before the mainshock (Fig. 6d). For D1, we observe a nearly-monotonic increase in V_p/V_s before the mainshock with a cumulative change of $\sim$ 10% (Figs. 6e and 7a). In contrast, the V_p/V_s ratio of D2 dropped by $\sim$ 5% between $\sim$ 30 and $\sim$ 80 d and then gradually increased by $\sim$ 4% in the remaining time before the mainshock (Figs. 6f and 7a). The changes in V_p/V_s ratio in the barrier-zone (Figs. 1b and 6c–f) may be related to pore-fluid migration or slip transients as suggested by the intense foreshocks in the barrier zone (McGuire et al., 2012; Gong & Fan, 2022).

4.3 3D Synthetic Tests

4.3.1 Validation of Spatial Variation

In-situ V_p/V_s ratio estimates are generally free of biases if the earthquakes have an isotropic distribution and the V_p/V_s ratio varies smoothly with depth (Lin & Shearer, 2007). Nonetheless, complex three-dimensional (3D) velocity structures may bias the estimates, although such effects depend on the velocity structure, event distribution, and network configuration (Palo et al., 2016). At G3, the barrier zone has a significantly lower V_p compared to the surrounding oceanic lithosphere (Roland et al., 2012), and our results as well as previous studies also suggest a strong along-strike velocity variation (Froment et al., 2014; Guo et al., 2018). Furthermore, the earthquakes are primarily distributed along strike with a narrow strike-normal spread (Fig. 1a). Given these complications, we perform synthetic tests using 3D velocity models to evaluate their effects on the in-situ V_p/V_s-ratio estimates.

We test three 3D velocity models consisting of a vertical fault zone embedded in the oceanic lithosphere (Figs . 8, 9, and S1). The oceanic lithosphere has the same 1D V_p profile as the one used for locating the earthquakes (Figs. 8a, 9a, and S1a; Gong and Fan (2022)). We set the V_p/V_s ratio of the oceanic lithosphere to decrease exponentially from 2.00 at the seafloor to 1.73 at infinite depth (Figs. 8b, 9b, and S1b). This V_p/V_s-ratio profile is consistent with those of the oceanic lithosphere derived from active-source experiments (e.g., Spudich & Orcutt, 1980). The fault zone has a uniform, low V_p of $5\,\mathrm{km\,s^{-1}}$ in all the models, which is obtained from Roland et al. (2012) (Figs. 8a, 9a, and S1a). The fault zone is extended to 10 km deep (Figs. 8a and b, 9a and b, and S1a and b) to match the deep seismicity in D1 and D2 (Figs. 1b–d). To assess the effects of the event and station distributions, we use the same station locations and the same earthquakes that are used for estimating the in-situ V_p/V_s ratios (Figs. 8a–c, 9a–c, and S1a–c). We compute synthetic P and S travel times using PyKonal (White et al., 2020), which can efficiently compute travel times and ray paths in 3D models. We then estimate the V_p/V_s ratios from the the synthetic travel times and compare them with the input values (Figs. 8d, 9d, and S1d).

Model 1 has a homogeneous fault zone with a V_p/V_s ratio of 1.70 and a width of 5 km (Figs. 8a–c), which is similar to the fault-zone width reported in Roland et al. (2012). The results show that the V_p/V_s-ratio estimates are close to the input value despite being slightly elevated on average (Fig. 8d). The deviations of the estimated values are smaller than 2% from the input values and show no spatial pattern (Fig. 8d). The small deviations are likely due to the smearing effects from the wall rock, which has a higher V_p/V_s ratio at the depths of the events ($\sim$ 1.75; Figs. 8b and c). These results demonstrate that the observed V_p/V_s-ratio contrast between the barrier zone and the mainshock zone is unlikely an artifact due to the source-receiver configuration.

In Model 2, we use a fault zone width of 5 km and assign a low V_p/V_s ratio of 1.70 to the western fault zone, which contains S1, S2, T, M1, and M2, and a high V_p/V_s ratio of 1.80 to the eastern fault zone, which contains F1, F2, D1, D2, and E (Figs. 9b and c). This V_p/V_s-ratio contrast imitates the observed V_p/V_s-ratio difference between the mainshock zone and the barrier zone (Fig. 1d). The fault zone is kept to have a homogeneous V_p of $5\,\mathrm{km\,s^{-1}}$ (Fig. 9a). We find that the contrast in V_p/V_s ratio between the two segments are well recovered (Fig. 9d). Similar to Model 1, smearing effects from the wall rock likely cause the V_p/V_s ratios of the western and eastern segments to be slightly overestimated and underestimated, respectively (Fig. 9d). These results demonstrate that given the source-receiver configuration, an along-strike V_p/V_s-ratio variation similar to the observation can be resolved with our method.

To assess the resolution of our method, we set Model 3 to have the same along-strike V_p/V_s-ratio variation as Model 2 but a fault-zone width of 2 km (Figs. S1a–c). This value is the lower bound of the fault-zone width reported in Roland et al. (2012). For this case, the estimated V_p/V_s ratios of all fault patches are close to 1.75, the V_p/V_s ratio of the wall rock at the event depths, without a clear difference between the two segments (Fig. S1d). This example highlights that the smearing effect of the surrounding materials can significantly affect the V_p/V_s-ratio estimates of the fault-zone materials when the fault zone is too narrow. We will further discuss the uncertainty caused by 3D velocity structures in Section 5.1.2.

4.3.2 Validation of Temporal Variation

We further design Model 4 and Model 5 to validate the the apparent V_p/V_s-ratio increase in the barrier zone (F1, F2, and D1). Specifically, we compute the synthetic travel times for the first and the last time windows of the three patches using the true event locations. We then estimate the V_p/V_s ratios using the synthetic data and compare them with the input values. We set Model 4 to have the same velocity structure as Model 1 at both the first and last time windows, i.e., Model 4 is time invariant (Fig. 10a). The estimated V_p/V_s ratios show no change over time, although the values of both time windows are slightly overestimated as observed in the case of Model 1 (Figs. 8d and 10a). These results demonstrate that the observed temporal change in V_p/V_s ratio in the barrier zone (F1, F2, and D1) is unlikely an artifact caused by a change in event distribution over time. Finally, we use Model 5 to test the resolvability of a temporal change in V_p/V_s ratio similar in size and duration to the observations. Model 5 has the same velocity structure as Model 1 in the first time window and changes to Model 2 in the second window, i.e., the V_p/V_s ratio of the eastern fault zone increases from 1.70 to 1.80 (Fig. 10b). We find that the V_p/V_s-ratio changes of all three patches are well recovered with marginal differences from the input values (Fig. 10b). These two tests show that the observed V_p/V_s-ratio increase in the barrier zone is unlikely an artifact and that an V_p/V_s-ratio increase in the barrier zone is resolvable with our method and data.

5 Discussions

5.1 Uncertainty Analyses

We evaluate uncertainties in the in-situ V_p/V_s-ratio estimates resulting from two main sources: noise and model assumptions.

5.1.1 Uncertainty from Noise

The noise in the differential arrival-time data has three major components: instrument clock drifts, event-timing errors, and cross-correlation alignment errors. Although the linear time drifts in the OBS data were removed (Gouédard et al., 2014), significant nonlinear time drifts may still be present and could bias the V_p/V_s ratio estimates. To evaluate the potential impacts of instrument clock drifts, we estimate the V_p/V_s ratios for the five fault patches in the mainshock zone and barrier zone (M1, M2, F1, F2, D1, and D2) using different maximum temporal separations between event pairs of 15, 30, 45, and 60 days (Fig. 11). The results show that the V_p/V_s ratio estimates decrease slightly ($< 4\%$) with increasing maximum event temporal separation, although the relative difference between the patches largely remains the same (Fig. 11). Event pairs with large event temporal separations likely suffer greater errors due to clock drifts. Such instrument clock drifts introduce the same bias to both the P and S differential arrival times, causing the V_p/V_s ratio estimates to converge towards 1, which may explain the negative correlation between the estimated V_p/V_s ratios and the maximum event temporal separation. Given that the V_p/V_s ratios estimated using the preferred maximum event temporal separation (30 days) do not differ significantly from those estimated using a smaller maximum event temporal separation (15 days; Fig. 11), we conclude that the results are unlikely biased by instrument clock drifts.

In theory, event-timing errors can be estimated and removed from the data. However, other types of noise, especially the cross-correlation alignment errors, can complicate corrections for such errors in reality. As the first step of the quality-control process, removing differential arrival times with low cross-correlation values (< 0.6; Fig. 3) cannot fully eliminate cross-correlation measurement errors, which is likely due to misalignment between different phases (e.g., P and S; Fig. S2). Microearthquakes typically have short body wave pulses, and bandpass-filtered P and S waves may have similar waveforms. For example, aligning a P phase with the associated S phase will yield an erroneous differential arrival time but a high cross-correlation value, causing outliers in the measurements (Fig. 2a). We thus designed the linearity step in the preprocessing procedure to further eliminate these outliers while also removing the event-timing errors (Figs. 3 and 4).

Since the preprocessing procedure removes the majority of the measurements (Fig. 2), one concern is if this procedure could bias the estimated V_p/V_s ratios. To evaluate this possibility, we generate differential P and S arrival times assuming a V_p/V_s ratio of 2.00, an extreme value for rocks, and add synthetic event-timing errors, Gaussian random noise, and outliers step by step to generate three sets of synthetic data (Fig. 12). The event-timing errors and Gaussian noise are randomly generated from Gaussian distributions with a zero mean and standard deviations of 0.02 and 0.01 s, respectively, and the outliers are simulated by contaminating 1% of the P and S differential arrival times with random noise generated from a uniform distribution between -0.2 and 0.2 s. We then apply the preprocessing and robust slope estimation procedures to these data and compare the estimated slopes with the input value (Fig. 12). The results show that in all three cases, the estimated slopes perfectly match the input slope. We also perform the same test on differential arrival times generated assuming a V_p/V_s ratio of 1.30, another extreme value for rock s, which also shows a very good agreement between the estimated and input slopes (Fig. S3). These tests demonstrate that the preprocessing procedure does not bias the V_p/V_s-ratio estimates.

A common way to estimate the uncertainty of in-situ V_p/V_s ratios is the bootstrap-resampling method (e.g., Lin & Shearer, 2007). This method quantifies the coherency of a given set of differential arrival times. However, the uncertainty given by bootstrap resampling is likely an underestimate because it does not account for the uncertainty associated with the data-selection procedure (Fig. 2). Therefore, in addition to bootstrap resampling, we also performed sensitivity tests on $\mathrm{N_{min}}$, $\mathrm{RMS_{max}}$, and τ_{min}, three key parameters of the preprocessing procedure, to evaluate their effects on the V_p/V_s-ratio estimates. The results show that the difference in V_p/V_s ratio between the barrier zone and the mainshock zone is a robust feature regardless of parameter choice (Fig. 5).

5.1.2 Uncertainty from Model Assumptions

The in-situ V_p/V_s-ratio method implicitly assumes that the P and S waves from an event pair share the same ray path (Lin & Shearer, 2007), which is inaccurate in regions with strong 3D variations in V_p/V_s ratio. We thus used realistic 3D velocity models to evaluate their effects on the V_p/V_s ratio estimates (Figs. 8, 9, and S1). We showed that the V_p/V_s-ratio estimates of the fault zone can be biased towards the V_p/V_s ratio of the wall rock (smearing effects) and that the degree of bias depends on the width of the fault zone (Figs. 8, 9, and S1). Using event pairs with a smaller spatial separation could reduce the smearing effects and increase the spatial resolution. However, a small spatial separation would cause a narrower range of differential times and thus less reliable slope and intercept estimates (Fig. 4). Therefore, the choice of maximum inter-event separation likely controls the trade-off between estimation precision and accuracy. The synthetic tests also show that we can reliably resolve the relative difference in V_p/V_s ratio between different fault segments and time windows. The identified V_p/V_s-ratio contrast between the barrier zone and the mainshock zone likely exists, although the absolute value of the contrast may have been underestimated, similar to the conclusion of Bloch et al. (2018), which also used a comprehensive 3D synthetic test to verify their in-situ V_p/V_s-ratio observations.

5.2 Comparison with Previous Tomography Results

The tomography models of Guo et al. (2018) show a strong lateral variation in velocities in the G3 fault zone. The tomography models, including a V_p/V_s-ratio model, are obtained using the same OBS waveform data but a different earthquake catalog (Guo et al., 2018; Gong & Fan, 2022). The V_p/V_s-ratio model of Guo et al. (2018) suggests a greater range of V_p/V_s-ratio variation (∼1.5–2.1) than our results (∼1.6–1.8; Fig. S4). Both studies agree qualitatively on the high V_p/V_s ratio in F2 and the low V_p/V_s ratios in T, M1, and M2 (Fig. S4). In contrast, Guo et al. (2018) does not observe high V_p/V_s ratios in F1, D1, and D2 as shown by our results (Fig. S4). The comparison in E may not be meaningful because both models have lower resolutions in the region. The tomography model shows a high V_p/V_s ratio above ∼4 km depth in the distance ranges −30–−13 km and ∼−7–5 km along strike, which are not resolved in our results (Fig. S4).

The apparent differences between our results and those from Guo et al. (2018) may be due to the differences in sensitivity between our method and the tomographic-inversion approach used in Guo et al. (2018). Our method directly estimates the V_p/V_s ratio in a compact earthquake cluster by solving an over-determined problem of fitting a line to the differential arrival times, which is likely to yield a robust result. The small footprints of earthquake clusters also provide a high spatial resolution. In contrast, Guo et al. (2018) used differential arrival times to solved for the V_p/V_s ratios on a mesh of dense grid points in the volume occupied by their event pairs. Although such a method may offer a higher spatial resolution, the ill-conditioned problem requires smoothing and regularization to stabilize the inversion (Guo et al., 2018). The models of Guo et al. (2018) may provide constraints on the material properties of the shallow part of the barrier zone where earthquakes are sparse. The collective observations of both studys suggest an elevated V_p/V_s ratio in the entire barrier zone, consistent with sea-water infiltration down to the upper mantle in the barrier zone, causing the deep seismicity in D1 and D2 (McGuire et al., 2012).

5.3 Physical State of G3 Fault Zone

5.3.1 Fault-Zone Structural Complexity

The percentage of the measurements passing the preprocessing procedure, defined as retention rate, may also offer information about the structural complexity in the fault zone. In the CC step, D1 and D2 show a high retention rate of 40–50 %; M1, M2, F1, F2, and E show an intermediate retention rate of 15–35 %; S1, S2, and T show a low retention rate of <10 % (markers with light-gray edges in Fig. 13). The linearity-step retention rates generally correlate with the CC-step retention rates except for D1 and D2, though the linearity-step retention rates are significantly lower (< 10%; markers with dark-gray edges in Fig. 13). The retained events in F2 are mostly located in the deep part of the patch (Fig. 1d), suggesting a possible difference between the shallow and deep parts of F2. The data retention rate of the CC step is a proxy of the waveform similarity between nearby events, which is analogous to the waveform similarity coefficient defined in Trugman et al. (2020). The different data retention rates of different fault patches might be caused by a variation in medium complexity, with a higher medium complexity causing a higher waveform complexity, which results in cross-correlation results with lower quality and thus a lower retention rate. Medium complexity includes both stress and structural heterogeneity (e.g., material heterogeneity and fault networks), which are closely related. Particularly, the low retention rate of F2 might be due to its high degree of fracturing, especially in its shallow portion (Fig. 13), which could have enabled hydrothermal circulation to produce a highly heterogeneous velocity structure. Such a fluid-saturated fault zone could have strong dilatency effects, which could have been the physical cause of the barrier zone repeatedly stopping the $M6$ ruptures on the adjacent fault segments (Liu et al., 2020).

5.3.2 Physical Models of Fluid-Saturated Rocks

Variations of V_p/V_s ratio in the oceanic lithosphere have long been associated with the presence of pore fluids (e.g., Spudich & Orcutt, 1980; Barclay et al., 2001; Bloch et al., 2018), and both fluid fraction and pore geometry were known to control the V_p/V_s ratios of water-saturated rocks (e.g., Shearer, 1988; Lin & Shearer, 2009). To investigate the physical causes of the observed in-situ V_p/V_s ratios, we examine the effects of fluid fraction and pore geometry by building idealized porous-medium models and comparing their predictions with the observations. We assume an intact rock matrix with randomly oriented spheroidal pores filled with water, which is characterized by the fluid volume fraction ϕ ($0 < \phi < 1$) and the aspect ratio of the spheroidal pores ϵ ($0 < \epsilon < 1$). For each combination of ϕ and ϵ, we follow Berryman (1980) to construct a self-consistent model to compute the effective V_p/V_s ratio of the medium. Our model requires the elastic parameters and densities of the rock matrix and water. For the rock matrix, we choose two representative rock types for oceanic crust and upper mantle, namely diabase (Alt et al., 1993) and harzburgite (Lippard, 1986). Their physical properties are adjusted to a temperature and pressure condition of 600 °C and 150 MPa following Abers and Hacker (2016) (hereafter, the physical properties mentioned are all for 600 °C and 150 MPa unless specified otherwise). We obtain the bulk modulus and density of high-temperature-and-pressure water from the specific volume and entropy data in Tödheide (1972). The physical properties of the rock matrices and water at the assumed temperature and pressure are summarized in Table S2.

We compute the effective V_p/V_s ratios of porous rocks as functions of fluid volume fraction in the range 0–0.1 assuming different pore aspect ratios for both diabase and harzburgite (Fig. 14). The volume-fraction range is derived from Roland et al. (2012), which suggests the barrier zone having a porosity of $\sim$8%. We find that in the case of a small pore aspect ratio ($\epsilon < 0.02$; thin cracks), the effective V_p/V_s ratio first decreases then increases with increasing fluid volume fraction, whereas in the case of a large pore aspect ratio ($\epsilon > 0.02$; thick cracks), the effective V_p/V_s ratio decreases with increasing fluid fraction (Fig. 14). Our results are consistent with the predictions of similar models from previous studies (e.g., Shearer, 1988). The effective V_p/V_s ratios of the diabase model and the harzburgite model show the the same relation with fluid fraction and pore aspect ratio except that the former is greater than the latter due to a greater V_p/V_s ratio for intact diabse (1.81) than intact harzburgite (1.73; Fig. 14).

5.3.3 Comparison between In-situ V_p/V_s Ratios and Physical-model Predictions

We compare the V_p/V_s-ratio estimates for F1, F2, M1, and M2 with the predictions of the diabase model because these patches are located in the crust and compare the estimates for D1 and D2 with the predictions of the harzburgite model because they are likely located in the upper mantle (Fig. 14). The V_p/V_s-ratio estimates of the fault patches fluctuated during the observation period (Figs. 6 and 7), which may reflect changes in fluid fraction and pore aspect ratio. We thus use the minimum and maximum V_p/V_s-ratio estimates as the reference values for each fault patch and compare them with the predictions of the physical models (Fig. 14). For F1 and F2, their minimum V_p/V_s ratios are close to the lower bound of all models and are only consistent with the model with $\epsilon =\sim 0.05$ and $\phi =\sim 0.08$. The maximum V_p/V_s ratios of the two fault patches are close to the V_p/V_s ratio of intact diabase and can be explained with models with a wide range of ϵ and ϕ (Fig. 14a). Intriguingly, the V_p/V_s-ratio ranges of M1 and M2 are below the lower bound of all models (Fig. 14a). For the mantle patches, the minimum V_p/V_s ratios of D1 and D2 are consistent with a wide range of ϕ and ϵ, whereas their maximum values can only be explained by models with a high fluid volume fraction ($\phi > 0.06$) and a small pore aspect ratio ($\epsilon < 0.02$; Fig. 14b).

Our V_p/V_s-ratio estimates at G3 can generally be explained by porous-medium models with a reasonable fluid volume fraction, which are consistent with other geophysical evidence (Roland et al., 2012). However, the fluid volume fraction cannot be independently determined due to its coupled effects with pore geometry, which is largely unknown (e.g., pore aspect ratio; Fig. 14). Nonetheless, the fluid fraction and pore geometry of the G3 fault zone can be independently constrained by searching for parameter combinations that match both the V_p and V_p/V_s ratios or by incorporating electromagnetic observations, which are also sensitive to pore fluids. (e.g., Takei, 2002; Naif et al., 2015).

The porous-medium models show that the V_p/V_s ratios of M1 and M2 are too low to be caused by pore fluids alone and thus require other physical mechanisms (Fig. 14a). Thermal structure of oceanic transform faults varies gradually along strike (Roland et al., 2010) and thus is unlikely the cause of the sharp V_p/V_s-ratio contrast between the mainshock zone and the barrier zone (Fig. 1d). Furthermore, neither diabase nor harzburgite shows a significant change in V_p/V_s ratio within the possible temperature range (Fig. S5; Abers & Hacker, 2016). Chemical alteration may strongly affect the V_p/V_s ratio of the fault-zone materials. However, Roland et al. (2012) ruled out the presence of a significant amount of serpentine in the G3 barrier zone based on gravity measurements. Therefore, we speculate that other metamorphic minerals from reactions between the basaltic crustal rocks and sea water may have caused the low V_p/V_s ratios of M1 and M2. Specifically, low-grade metamophic reactions could transfer anorthite in basaltic rocks into minerals with lower V_p/V_p ratios, such as zeolite (1.77), prehnite (1.73), and epidote (1.63) (Best, 2003). Such processes would systematically reduce the V_p/V_p ratios of M1 and M2, effectively shifting the curves in Fig. 14 downward, and the V_p/V_s-ratio estimates of M1 and M2 would be consistent with models with large pore aspect ratio (thick cracks; Fig. 14a). In this case, the sharp contrast in V_p/V_s ratio between the mainshock zone and the barrier zone (Fig, 1d) could be due to a combined effect of pore fluids and chemical alteration. These inferences of fault-zone material properties will benefit from further petrological and petrophysical investigations on the materials in the Gofar fault zone.

The temporal evolution of the V_p/V_s ratios in F1, F2, D1 and D2 within a few months before the mainshock is unlikely due to a change in mineral composition because metamorphic reactions occur much more slowly (Figs. 6c–f). Therefore, these temporal changes in V_p/V_s ratio are likely due to perturbations of pore fluids. The idealized porous-medium models suggest that a decrease in pore aspect ratio (i.e. thick cracks transitioning into thin cracks) and an increase in fluid fraction can cause an increase in V_p/V_s-ratio, which may explain the nine-month V_p/V_s-ratio increase observed for F1, F2, D1, and D2 (Fig. 14).

Fluid migration can affect both fluid fraction and pore aspect ratio while causing seismic and aseismic slips (Huang et al., 2019; Ross et al., 2020). Besides, shear sliding can alter pore spaces via dilatancy effects (Liu et al., 2020), which may couple with fluid migration to influence the V_p/V_s ratios in the fault zone. Our findings suggest that in-situ V_p/V_s ratios can be used to monitor the physical state of fault-zone materials at great spatial and temporal resolutions.

6 Conclusions

We develop a new method to compute in-situ V_p/V_s ratios using differential arrival times of nearby earthquakes. We apply this method to ocean-bottom-seismometer data at the westernmost Gofar transform fault and find that the fault zone material has a robust along-strike variation in V_p/V_s ratio, with the eastern segment, which includes the barrier zone, having a moderate V_p/V_s ratio of 1.75–1.80 and the western segment, which includes the down-dip edge of the 2008 $M6$ earthquake, having a low V_p/V_s ratio of 1.61–1.69. This variation may be caused by differences in pore fluids and chemical alteration. We also observe a nine-month V_p/V_s-ratio increase in the barrier zone, which may be caused by a combined effect of an increasing number of thin cracks and increasing fluid fraction. Our results suggest that the in-situ V_p/V_s-ratio method is a useful tool for monitoring the physical state of fault-zone materials.

7 Open Research

The waveform data are downloaded from the Data Management Center (DMC) of the Incorporated Research Institutions for Seismology (IRIS) under the network codes ZD. The metadata of the network can be accessed at `https://ds.iris.edu/mda/ZD/?starttime=2007-01-01T00:00:00&endtime=2009-12-31T23:59:59`. The earthquake catalog is from Gong and Fan (2022) (DOI:10.1002/essoar.10511753.1). The bathymetry data are obtained from `https://www.ngdc.noaa.gov/maps/autogrid/`. The SciPy TLS package is described at `https://docs.scipy.org/doc/scipy/reference/odr.html`. Pykonal is available at `https://github.com/malcolmw/pykonal`.

Acknowledgments

T.L. is supported by National Science Foundation (NSF) grants EAR 1829601 and EAR 2123529 and a Green Postdoctoral Scholarship. J.G. and W.F. are supported by NSF grants OCE-1833279 and EAR-2143413. G.L. is supported by EAR-2022429. The ocean bottom seismometer instruments were provided by the Ocean Bottom Seismograph Instrument Center (OBSIP). We thank Malcolm White for helping us use PyKonal and Geoffrey Abers for helping us calculate physical properties of rocks at high temperatures and pressures. We thank Hao Guo for sharing the data file of the model in his paper. We thank Jeffrey McGuire, John Collins, and the rest of the 2008 Quebrada-Discovery-Gofar experiment team for collecting and archiving the data. IRIS Data Services are funded through the Seismological Facilities for the Advancement of Geoscience and EarthScope (SAGE) Proposal of the National Science Foundation (NSF) under Cooperative Agreement EAR-1261681.

References

Abers, G. A., & Hacker, B. R. (2016). A matlab toolbox and e xcel workbook for calculating the densities, seismic wave speeds, and major element composition of minerals and rocks at pressure and temperature. *Geochemistry, Geophysics, Geosystems*, *17*(2), 616–624.

Alt, J. C., Kinoshita, H., Stokking, L., Allerton, S., Bach, W., Becker, K., . . . others (1993). Ocean drilling program leg 148, preliminary report hole 504b. *College*

Station, TX (Ocean Drilling Program).

Barclay, A. H., Toomey, D. R., & Solomon, S. C. (2001). Microearthquake characteristics and crustal vp/vs structure at the mid-atlantic ridge, 35 n. *Journal of Geophysical Research: Solid Earth*, *106*(B2), 2017–2034.

Berryman, J. G. (1980). Long-wavelength propagation in composite elastic media ii. ellipsoidal inclusions. *The Journal of the Acoustical Society of America*, *68*(6), 1820–1831.

Best, G., Myron. (2003). Mineral assemblages in mafic protoliths: A brief overview. In *Igneous and metamorphic petrology* (2nd ed., p. 587). Blackwell Science Ltd.

Bloch, W., John, T., Kummerow, J., Salazar, P., Krüger, O. S., & Shapiro, S. A. (2018). Watching dehydration: Seismic indication for transient fluid pathways in the oceanic mantle of the subducting nazca slab. *Geochemistry, Geophysics, Geosystems*, *19*(9), 3189–3207.

Boettcher, M. S., & McGuire, J. J. (2009). Scaling relations for seismic cycles on mid-ocean ridge transform faults. *Geophysical Research Letters*, *36*(21).

Christensen, N. I. (1996). Poisson's ratio and crustal seismology. *Journal of Geophysical Research: Solid Earth*, *101*(B2), 3139–3156.

Froment, B., McGuire, J., van der Hilst, R., Gouédard, P., Roland, E., Zhang, H., & Collins, J. (2014). Imaging along-strike variations in mechanical properties of the gofar transform fault, east pacific rise. *Journal of Geophysical Research: Solid Earth*, *119*(9), 7175–7194.

Gong, J., & Fan, W. (2022). *Seismicity, fault architecture, and slip mode of the westernmost gofar transform fault.* Retrieved from `https://doi.org/10.1002/essoar.10511753.1` (Unpublished Manuscript) doi: 10.1002/essoar.10511753.1

Gouédard, P., Seher, T., McGuire, J. J., Collins, J. A., & van der Hilst, R. D. (2014). Correction of ocean-bottom seismometer instrumental clock errors using ambient seismic noise. *Bulletin of the Seismological Society of America*, *104*(3), 1276–1288.

Guo, H., Zhang, H., & Froment, B. (2018). Structural control on earthquake behaviors revealed by high-resolution vp/vs imaging along the gofar transform fault, east pacific rise. *Earth and Planetary Science Letters*, *499*, 243–255.

Huang, Y., De Barros, L., & Cappa, F. (2019). Illuminating the rupturing of microseismic sources in an injection-induced earthquake experiment. *Geophysical Research Letters*, *46*(16), 9563–9572.

Lin, G., Amelung, F., Shearer, P. M., & Okubo, P. G. (2015). Location and size of the shallow magma reservoir beneath kīlauea caldera, constraints from near-source vp/vs ratios. *Geophysical Research Letters*, *42*(20), 8349–8357.

Lin, G., Peng, Z., & Neves, M. (2022). Comparisons of in situ v p/v s ratios and seismic characteristics between northern and southern california. *Geophysical Journal International*, *229*(3), 2162–2174.

Lin, G., & Shearer, P. (2007). Estimating local vp/vs ratios within similar earthquake clusters. *Bulletin of the Seismological Society of America*, *97*(2), 379–388.

Lin, G., & Shearer, P. M. (2009). Evidence for water-filled cracks in earthquake source regions. *Geophysical Research Letters*, *36*(17).

Lin, G., & Shearer, P. M. (2021). Spatiotemporal variations of focal mechanism and in situ vp/vs ratio during the 2018 kīlauea eruption. *Geophysical Research Letters*, *48*(18), e2021GL094636.

Lin, G., Shearer, P. M., & Hauksson, E. (2007). Applying a three-dimensional velocity model, waveform cross correlation, and cluster analysis to locate southern california seismicity from 1981 to 2005. *Journal of Geophysical Research: Solid Earth*, *112*(B12).

Lippard, S. J. (1986). The ophiolite of northern oman. *Geological Society London*

Memoir, *11*, 178.
Liu, Y., McGuire, J. J., & Behn, M. D. (2020). Aseismic transient slip on the gofar transform fault, east pacific rise. *Proceedings of the National Academy of Sciences*, *117*(19), 10188–10194.
McGuire, J. J. (2008). Seismic cycles and earthquake predictability on east pacific rise transform faults. *Bulletin of the Seismological Society of America*, *98*(3), 1067–1084.
McGuire, J. J., Boettcher, M. S., & Jordan, T. H. (2005). Foreshock sequences and short-term earthquake predictability on east pacific rise transform faults. *Nature*, *434*(7032), 457–461.
McGuire, J. J., Collins, J. A., Gouédard, P., Roland, E., Lizarralde, D., Boettcher, M. S., ... Van Der Hilst, R. D. (2012). Variations in earthquake rupture properties along the gofar transform fault, east pacific rise. *Nature Geoscience*, *5*(5), 336–341.
Naif, S., Key, K., Constable, S., & Evans, R. L. (2015). Water-rich bending faults at the m iddle a merica t rench. *Geochemistry, Geophysics, Geosystems*, *16*(8), 2582–2597.
Palo, M., Tilmann, F., & Schurr, B. (2016). Applicability and bias of vp/vs estimates by p and s differential arrival times of spatially clustered earthquakes. *Bulletin of the Seismological Society of America*, *106*(3), 1055–1063.
Roland, E., Behn, M. D., & Hirth, G. (2010). Thermal-mechanical behavior of oceanic transform faults: Implications for the spatial distribution of seismicity. *Geochemistry, Geophysics, Geosystems*, *11*(7).
Roland, E., Lizarralde, D., McGuire, J. J., & Collins, J. A. (2012). Seismic velocity constraints on the material properties that control earthquake behavior at the quebrada-discovery-gofar transform faults, east pacific rise. *Journal of Geophysical Research: Solid Earth*, *117*(B11).
Ross, Z. E., Cochran, E. S., Trugman, D. T., & Smith, J. D. (2020). 3d fault architecture controls the dynamism of earthquake swarms. *Science*, *368*(6497), 1357–1361.
Shearer, P. M. (1988). Cracked media, poisson's ratio and the structure of the upper oceanic crust. *Geophysical Journal International*, *92*(2), 357–362.
Spudich, P., & Orcutt, J. (1980). Petrology and porosity of an oceanic crustal site: Results from wave form modeling of seismic refraction data. *Journal of Geophysical Research: Solid Earth*, *85*(B3), 1409–1433.
Takei, Y. (2002). Effect of pore geometry on vp/vs: From equilibrium geometry to crack. *Journal of Geophysical Research: Solid Earth*, *107*(B2), ECV–6.
Tödheide, K. (1972). Water at high temperatures and pressures. In F. Franks (Ed.), *Water: A comprehensive treatise* (Vol. 1, pp. 464–482). Plenum Press.
Trugman, D. T., Ross, Z. E., & Johnson, P. A. (2020). Imaging stress and faulting complexity through earthquake waveform similarity. *Geophysical Research Letters*, *47*(1), e2019GL085888.
Van Huffel, S., & Vandewalle, J. (1991). *The total least squares problem: computational aspects and analysis.* SIAM.
White, M. C., Fang, H., Nakata, N., & Ben-Zion, Y. (2020). Pykonal: a python package for solving the eikonal equation in spherical and cartesian coordinates using the fast marching method. *Seismological Research Letters*, *91*(4), 2378–2389.

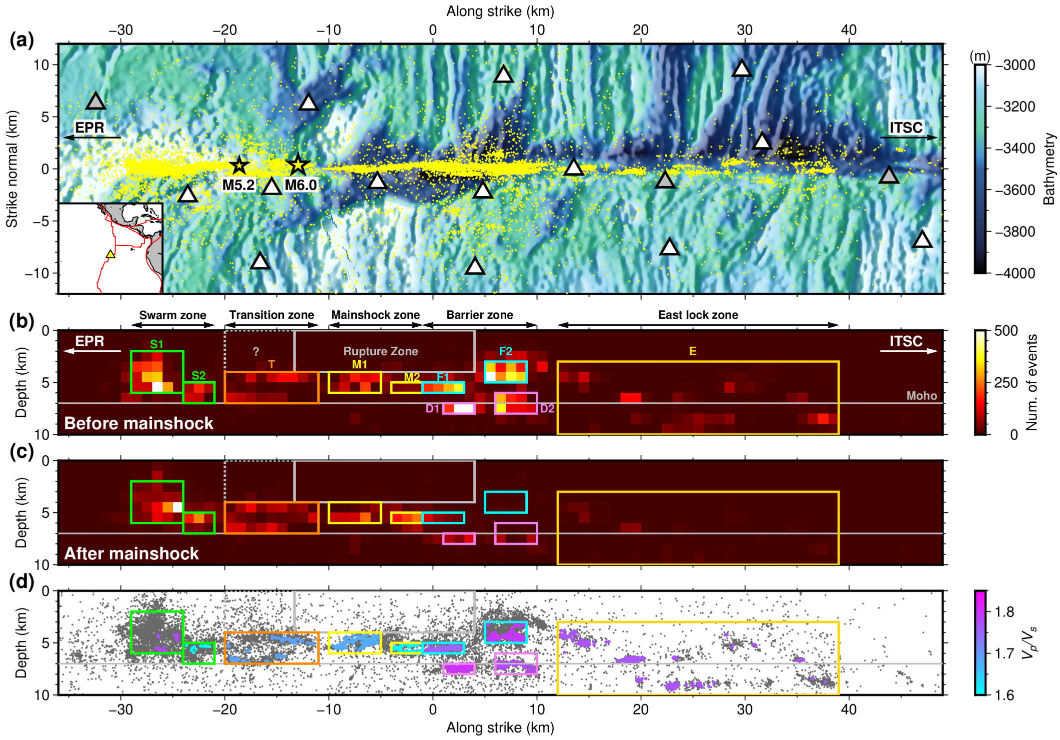

Figure 1. Summary of the observation geometry and the V_p/V_s-ratio estimates of each fault patch. The origin of the along-strike axis is approximately the same as the one in Figure 3 of McGuire et al. (2012). (a) Stations (triangles; functional and non-functional ones in white and gray, respectively) and events (yellow dots) plotted on the bathymetry of G3. Big and small stars: The $M6.0$ mainshock and the largest aftershock of $M5.2$. The East Pacific Rise (EPR) and an intra-transform spreading center (ITSC) are immediately west and east of the map boundaries, respectively. Inset: A regional map of the east Pacific showing the location of G3 (yellow triangle) and the plate boundaries (red lines). (b) Seismicity density on the fault plane before the mainshock, binned with $1\,\text{km} \times 1\,\text{km}$ grids. Rectangles with different colors mark different fault patches. Dashed gray rectangle: possible $M6$ rupture in the transition zone. (c) Similar to (b), but for the events after the mainshock. (d) Average V_p/V_s ratios of all fault patches. Gray dots: All events in Gong and Fan (2022). Colored dots: Events used for estimating the V_p/V_s-ratios, colored by the V_p/V_s ratios of the corresponding fault areas.

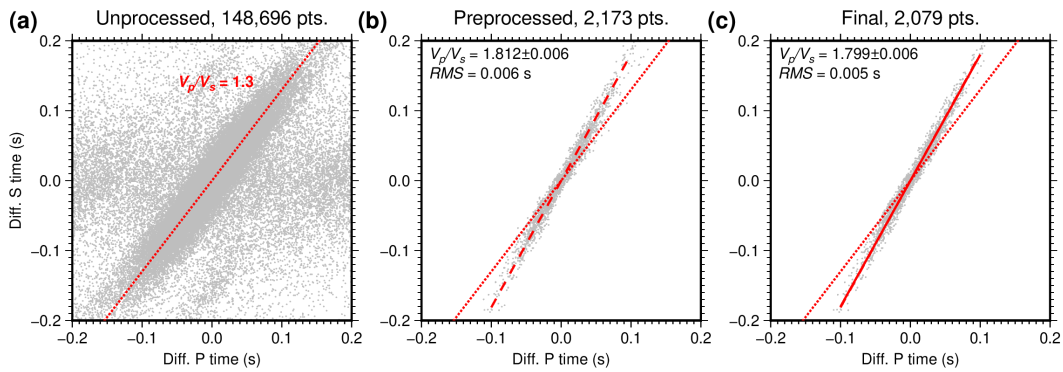

Figure 2. Differential P and S arrival times of the fault area D1 (Fig. 1b, c, and d) at three data-processing steps. Dotted red lines: Reference line with a slope of 1.3. Dashed red line: Line with a slope equal to the V_p/V_s ratio estimated using all preprocessed measurements. Solid red line: Line with a slope equal to the final estimated V_p/V_s ratio. (a) Unprocessed differential arrival times. (b) Differential arrival times after preprocessing. (c) Differential arrival times used for the final V_p/V_s-ratio estimation.

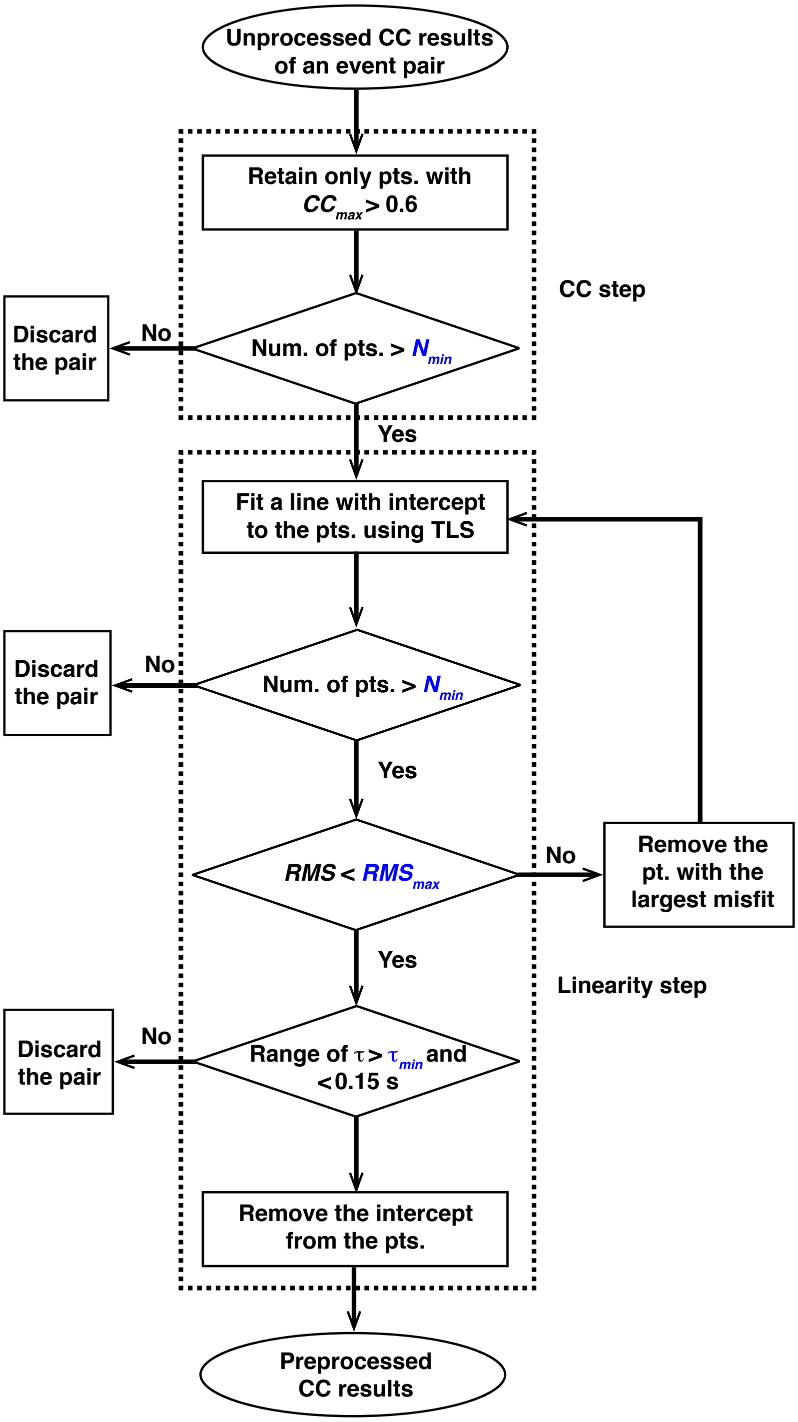

Figure 3. Summary of the preprocessing workflow. The key parameters tested in 5 are blue.

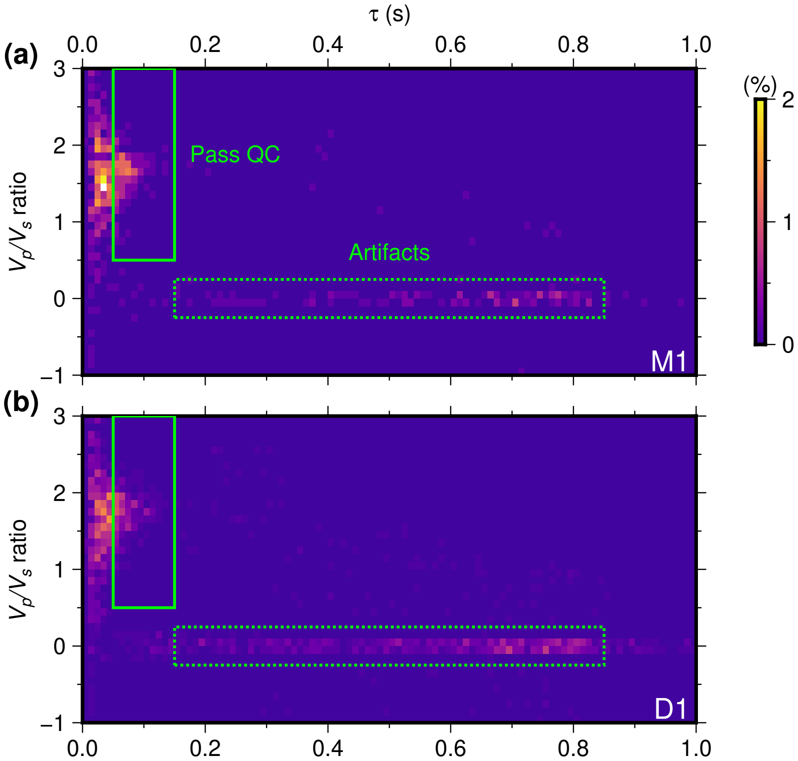

Figure 4. Joint distributions between the V_p/V_s ratios and differential-P-time ranges (τ) of the event pairs with intercept terms removed for (a) M1 and (b) D1. Solid green box: The preferred range of measurements for V_p/V_s ratio (0.5–3) and τ (0.05–0.15 s). Dotted green box: A cluster likely consisting of artifacts.

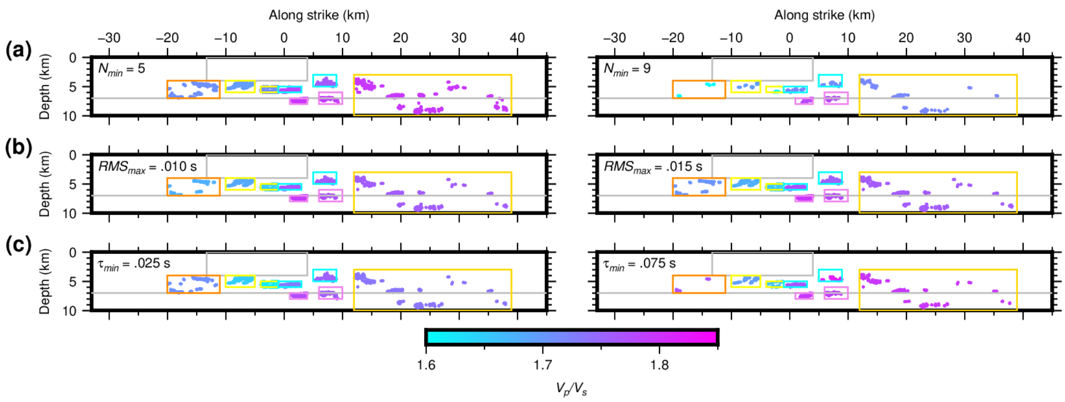

Figure 5. Effects of the three key preprocessing parameters N_{min}, RMS_{max}, and τ_{min} on the spatial pattern of the estimated V_p/V_s ratios. The two columns show the results of two alternate choices for (a) N_{min} (5 and 9), (b) RMS_{max} (0.010 and 0.015 s), and (c) τ_{min} (0.025 and 0.075 s) in comparison with the results of the preferred parameter choice shown in Fig. 1d. Colored dots and boxes are the same as the ones in Fig. 1d.

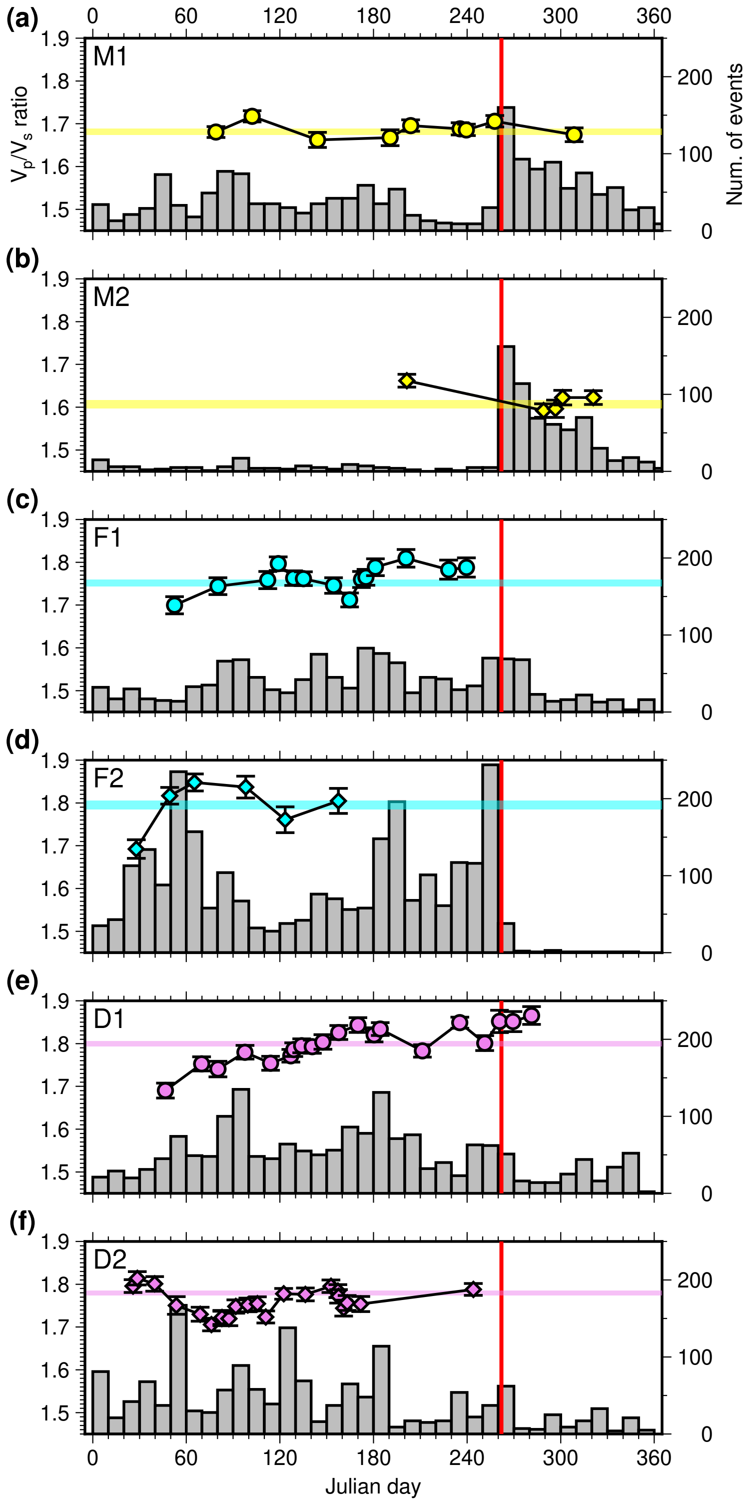

Figure 6. Temporal variations of the in-situ V_p/V_s ratios of (a) M1, (b) M2, (c) F1, (d) F2, (e) D1, and (f) D2. Colored markers: V_p/V_s ratio of each time window plotted at the center of the window. Colored bands: Uncertainty ranges of the temporal average V_p/V_s ratios. Gray histograms: Event counts with a 10-day bin width. Red vertical line: Time of the mainshock.

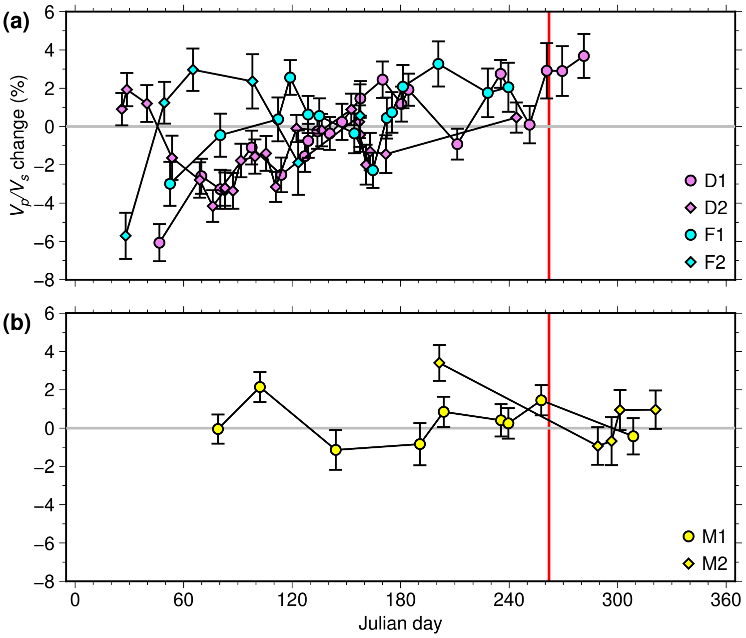

Figure 7. Percentage changes of the V_p/V_s ratios of (a) F1, F2, D1, and D2 and (b) M1 and M2. The changes are relative to the average V_p/V_s ratios of the respective fault patches.

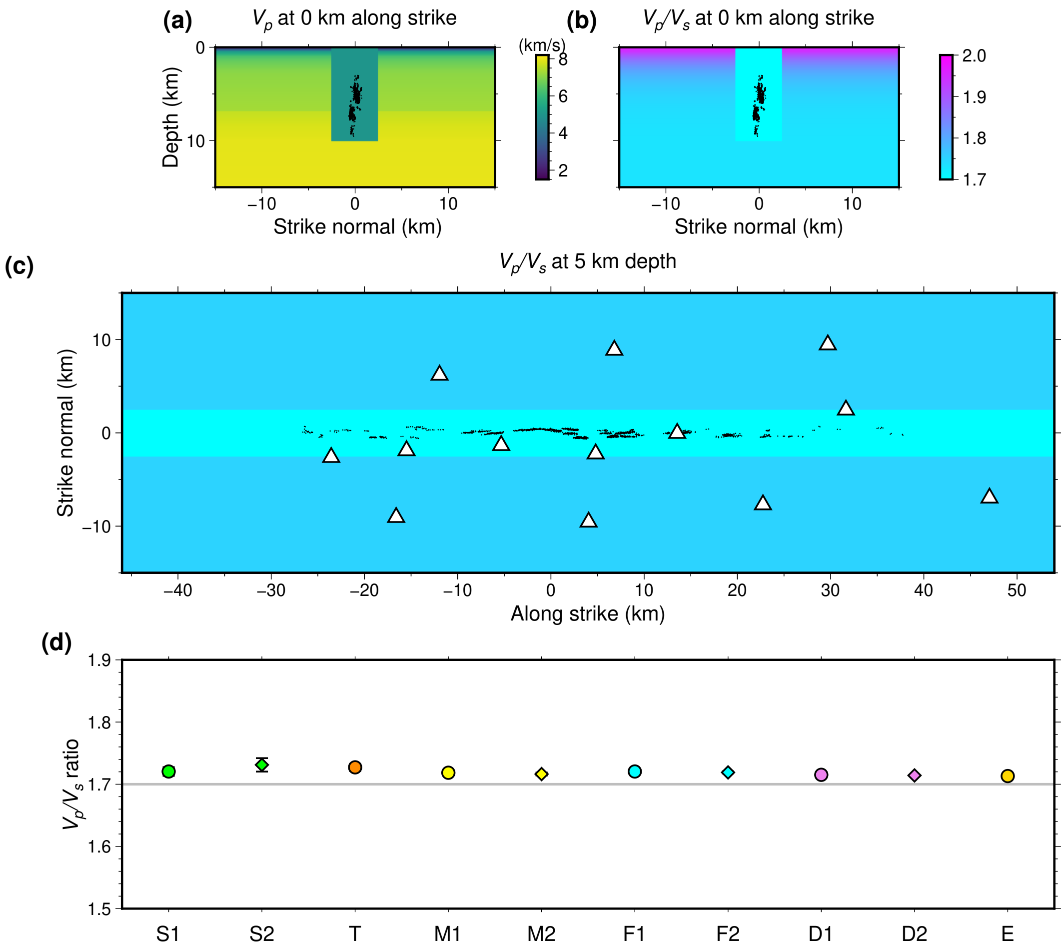

Figure 8. Summary of the 3D synthetic test assuming a homogeneous fault zone (Model 1). Black dots: Events used for the final V_p/V_s-ratio estimation. White triangles: Functional stations in 1a (a) Cross section of the V_p model at 0 km along strike. (b) Cross section of the V_p/V_s model at 0 km along strike. (c) Cross section of the V_p/V_s model at the depth of 5 km. (d) Retrieved V_p/V_s ratios of all fault patches (colored markers) compared with the input V_p/V_s ratio of the fault zone (gray line).

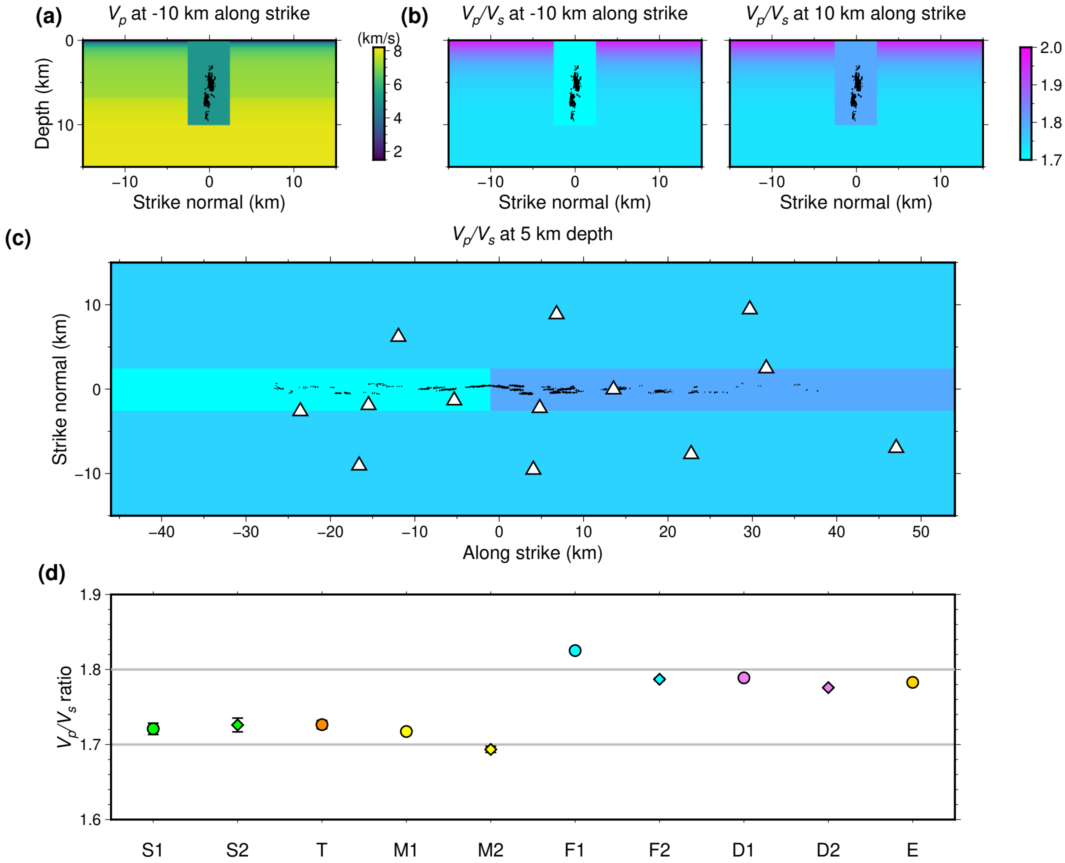

Figure 9. Similar to Fig. 8, but for the model with a segmented fault zone (Model 2). The gray lines in (d) mark the input V_p/V_s ratios of the two segments.

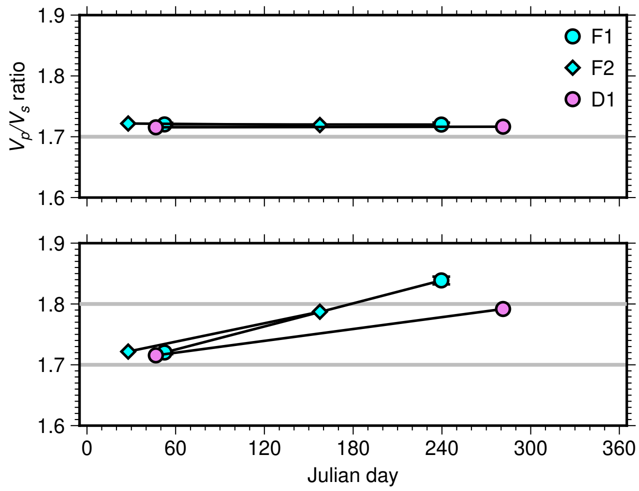

Figure 10. Synthetic tests of the temporal V_p/V_s-ratio increase in F1, F2, and D1. (a) Results for the case with Model 1 as the velocity model at both the first and second time windows. Colored markers: V_p/V_s-ratio estimates for the first and second time windows of the three patches of interest. Gray line: Input fault-zone V_p/V_s ratio. (b) Similar to (a) but for the case with Model 1 at the first window and Model 2 at the second window. Gray lines: Input fault-zone V_p/V_s ratios for the two time windows.

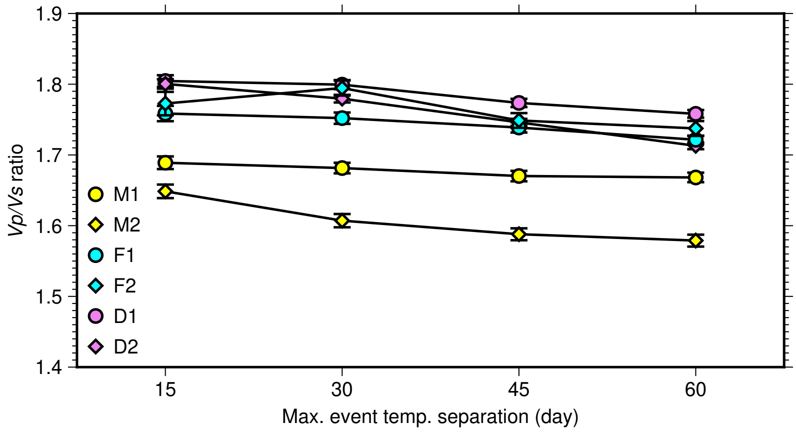

Figure 11. Effects of maximum temporal separation of event pairs on the V_p/V_s-ratio estimates for six fault patches. Colored markers: V_p/V_s ratios of different fault patches.

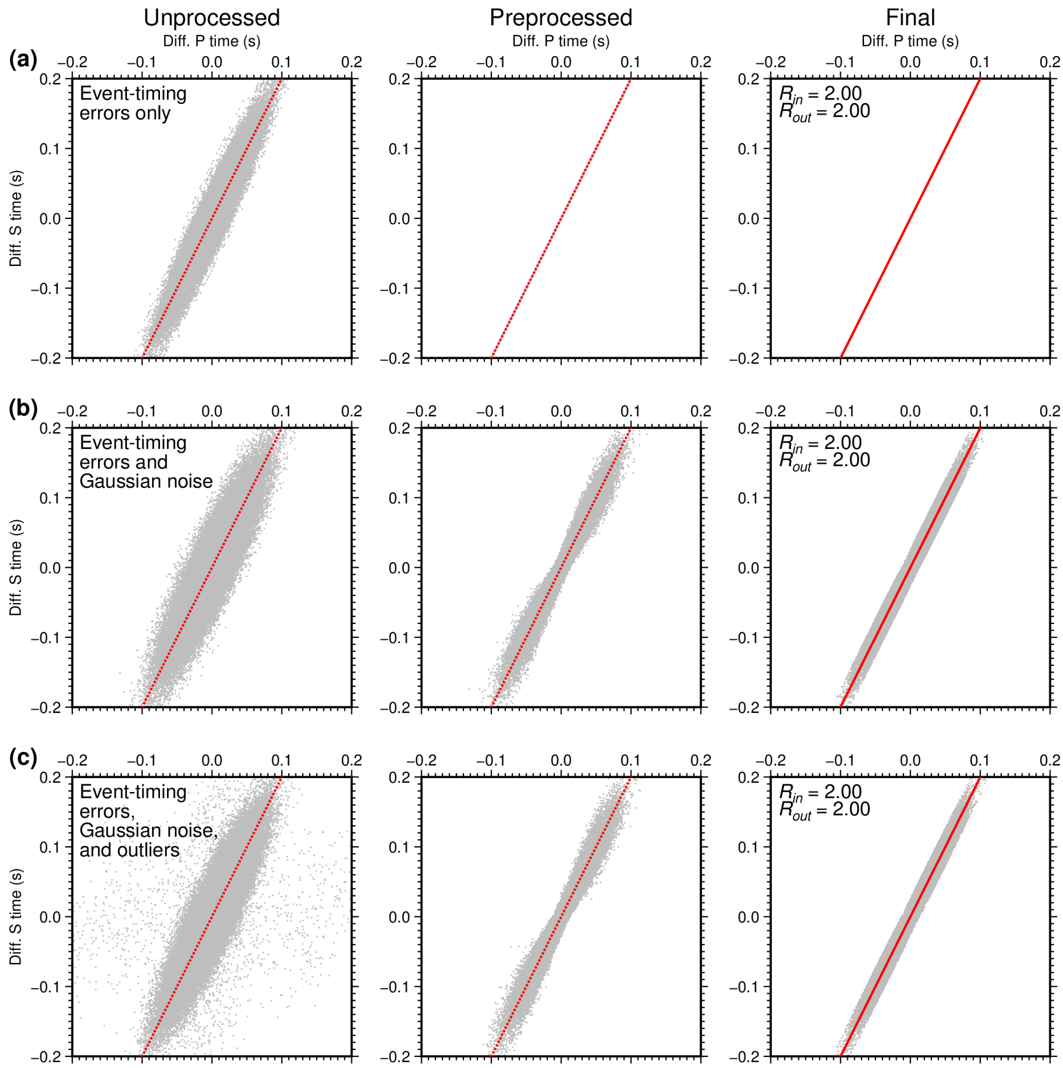

Figure 12. Synthetic tests of the effects of the preprocessing and robust-slope-estimation procedures. Dotted and solid red lines: Slope of the input noise-free data (2.00) and the slopes obtained from the estimation procedure, respectively. The three columns from left to right show input data points, the remaining data points after preprocessing, and the data points used for the final slope estimation, respectively. (a) Case with only event-timing errors. (b) Case with event-timing errors and Gaussian noise. (c) Case with event-timing errors, Gaussian noise, and outliers.

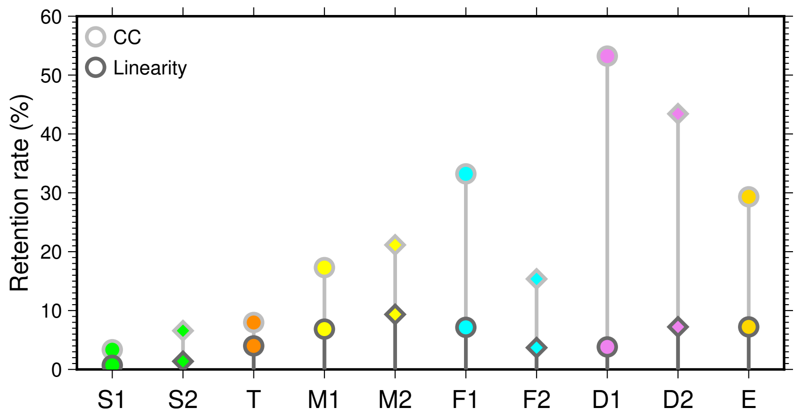

Figure 13. Data retention rates for all fault patches. The rates for the cross-correlation-value (CC) step and the linearity step are outlined in light and dark gray, respectively.

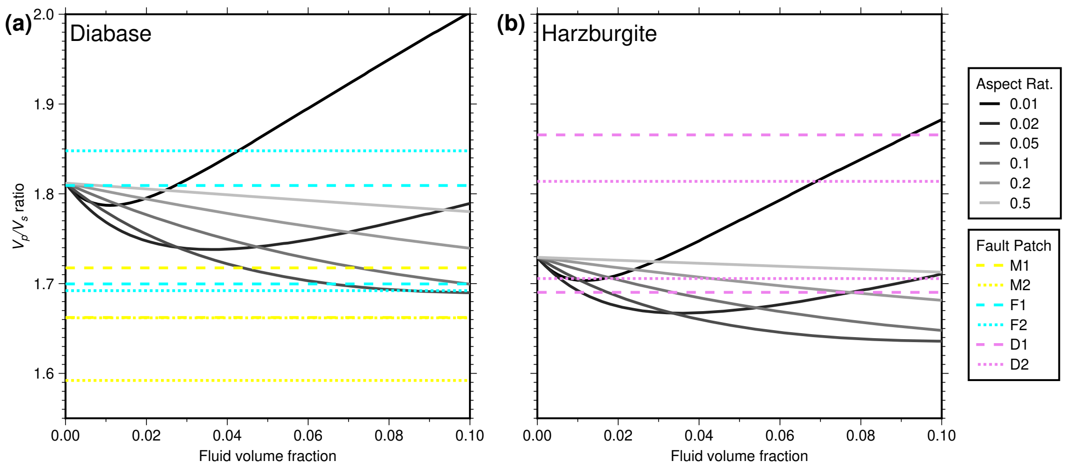

Figure 14. Physical models of effective V_p/V_s ratios of porous rocks for a rock matrix of (a) diabase (Alt et al., 1993) and (b) harzburgite. (Lippard, 1986). Black to light-gray curves: Models colored by their pore aspect ratios. Colored dashed and dotted lines: Ranges of the V_p/V_s ratio estimates for the six patches in the mainshock zone (M1 and M2) and the barrier zone (F1, F2, D1, and D2).